

Research Article

Melvin Liebsch*, Stephan Russenschuck and Stefan Kurz

BEM-Based Magnetic Field Reconstruction by Ensemble Kálmán Filtering

<https://doi.org/10.1515/cmam-2022-0121>

Received June 1, 2022; revised November 18, 2022; accepted November 20, 2022

Abstract: Magnetic fields generated by normal or superconducting electromagnets are used to guide and focus particle beams in storage rings, synchrotron light sources, mass spectrometers, and beamlines for radiotherapy. The accurate determination of the magnetic field by measurement is critical for the prediction of the particle beam trajectory and hence the design of the accelerator complex. In this context, state-of-the-art numerical field computation makes use of boundary-element methods (BEM) to express the magnetic field. This enables the accurate computation of higher-order partial derivatives and local expansions of magnetic potentials used in efficient numerical codes for particle tracking. In this paper, we present an approach to infer the boundary data of an indirect BEM formulation from magnetic field measurements by ensemble Kálmán filtering. In this way, measurement uncertainties can be propagated to the boundary data, magnetic field and potentials, and to the beam related quantities derived from particle tracking. We provide results obtained from real measurement data of a curved dipole magnet using a Hall probe mapper system.

Keywords: Boundary Element Methods, Particle Accelerator Magnets, Bayesian Inference, Data Assimilation, Magnetic Measurements

MSC 2010: 45Q05, 35Q62, 35Q61

1 Introduction

Static magnetic fields generated by electromagnets are used in particle accelerators to guide and focus particle beams. Studying the dynamics of the beam is indispensable in the design and operational phase of an accelerator complex and requires the accurate mathematical modeling of the magnetic fields. Preferably, the field model is an exact magneto-static solution obeying Maxwell's equations.

Hybrid models combine first principles modeling and data-driven modeling to improve the predictive accuracy while preserving the underlying physical relationships. In this way, the differences between the magnet model and the real physical object can be incorporated in the numerical field simulation and particle tracking while preserving the underlying physical nature.

Classically, the integrated field in an accelerator magnet is expressed by eigenfunctions of the Laplace equation in polar coordinates, so called *field harmonics*. It is common practice to measure the field harmonics by rotating induction-coil systems and to use the measurement results in particle tracking simulations. This approach combines first principles with measurement data and may therefore be regarded as a classical example of hybrid modeling.

The advantages of this method are far-reaching. One can exploit scaling laws derived from field harmonics to reconstruct the field based on measurements on a single radius while still maintaining an exact magneto-

*Corresponding author: Melvin Liebsch, CERN, TE-MS-C-TM, 1211 Meyrin, Switzerland, e-mail: melvin.liebsch@cern.ch.

<https://orcid.org/0000-0002-2022-105X>

Stephan Russenschuck, CERN, TE-MS-C-TM, 1211 Meyrin, Switzerland, e-mail: stephan.russenschuck@cern.ch.

<https://orcid.org/0000-0003-3370-7419>

Stefan Kurz, Faculty of Information Technology, University of Jyväskylä, 40014 Jyväskylä, Finland, e-mail: stefan.m.kurz@jyu.fi

static solution. Moreover, sensor systems can be designed particularly for the measurement of certain multipole components and specialized measurement equipment allows for the accurate determination of multipole errors even under the influence of mechanical vibration and shaft deformation [43].

In high energy physics, the particle beams are often contained in straight cylindrical vacuum chambers. In such cases the theory of field harmonics can be extended to three-dimensional cylindrical coordinates by generalized-gradients (see [36, Chapter 6], [37] and [47, Section 1.3.2]).

The motion of charged particles in the accelerator is computed numerically in particle tracking codes. The treatment of two-dimensional field harmonics is well established [47, Chapters 2 and 3]. The treatment of fringe fields and field inhomogeneities using generalized gradients was studied in [46], [34] and [5]. A more general and efficient approach based on a finite-element formulation was developed in [41].

In energy storage rings, beamlines for radiotherapy, mass spectrometers but also detector magnets, the fringe fields in the magnet ends give a relevant contribution to the equations of motion and particles might occupy more complex geometric domains. Hence, more general expressions for the magnetic field in the vacuum chamber are required. Boundary-element methods have been proposed as a field model to provide local expansions of the magnetic vector potential in the vicinity of a reference trajectory; [2, 10]. The local field description may be based on a Taylor approximation or an expansion into solid harmonics. An approach for the efficient treatment of such field descriptions in particle tracking is found in [48].

The quantitative characterization of uncertainties in model parameters due to random input data is the main objective of uncertainty quantification. Deterministic approaches for the uncertainty quantification for boundary-element methods with random right-hand sides are found in [8] and the references therein. Moreover, in [6] an approach for the shape inversion of a random scatterer, based on noisy measurement data is presented.

This article follows up on the advances of [21], but extends the analysis in four ways:

- A more general field representation by means of an indirect boundary-element method is adopted in order to cope with more general beamlines in particle accelerators and detectors.
- The efficiency of the Bayesian inference is enhanced by an ensemble Kálmán filter, where the statistics of the boundary data is expressed by means of an ensemble of state vectors. This approach is well known in the discipline of data assimilation, where the propagation of the full covariance matrix becomes infeasible due to the high dimension of the state space (see [4]).
- As rotating induction-coil measurements are tailored to cylindrical domains, a more flexible Hall probe mapper system is used, which allows us to sample the field locally within a larger class of physical domains. We derive a realistic noise model for this particular measurement system, which includes the effect of position errors and vibrations.
- An iterative learning algorithm is proposed that uses the spatial distribution of uncertainty in the predicted field to explore the spatial domain. This makes the inference of boundary data more effective, since measurements in regions with low uncertainty are reduced.

Section 2 of this paper covers the indirect boundary element method, employing a double layer potential that yields a "lightweight" physical representation for the magnetic vector potential. Section 3 then turns to the evaluation of measurement data, which is suffering from uncertainties. In Section 4 we give details about a real world application to which the partial results of Section 5 will be applied. Particularly, we consider the use-case of the field quality measurement of a strongly-curved dipole magnet. The main result of Section 5 is an ensemble Kálmán filter for the inference of boundary data. It bypasses the need for the propagation of the full posterior covariance matrix and thus enables the efficient uncertainty quantification.

2 The Indirect Double Layer Potential Formulation

Consider an open and simply connected Lipschitz domain Ω in the air gap, or vacuum chamber of an accelerator magnet, with boundary $\partial\Omega$. The domain is assumed to be free of magnetic sources in a way that the field is governed by the magneto-static equations

$$\operatorname{div} \mathbf{B} = 0, \quad \operatorname{curl} \mathbf{H} = \mathbf{0} \quad (2.1)$$

for the magnetic flux density \mathbf{B} and the magnetic field \mathbf{H} . In this case, the Laplace equation

$$\operatorname{div} \operatorname{grad} \phi_m = 0 \quad (2.2)$$

holds for the magnetic scalar potential ϕ_m , in Ω , which is defined via $\mathbf{B} = -\mu_0 \operatorname{grad} \phi_m$. Boundary integral equations can be derived from the Gauss integral theorem to represent the potential ϕ_m in Ω accordingly. Here we focus on the indirect representation formula, by using a *double-layer potential*

$$\phi_m(\mathbf{r}) = - \int_{\partial\Omega} \mathbf{n}(\mathbf{r}') \cdot \operatorname{grad}_{\mathbf{r}'} u^*(\mathbf{r}, \mathbf{r}') v(\mathbf{r}') d\mathbf{r}' := (Wv)(\mathbf{r}), \quad \mathbf{r} \in \Omega. \quad (2.3)$$

The vector \mathbf{n} is an outward directed unit vector, $u^*(\mathbf{r}, \mathbf{r}') = \frac{1}{4\pi} |\mathbf{r} - \mathbf{r}'|$ is the Green's function of free space, $\operatorname{grad}_{\mathbf{r}'}$ denotes the gradient operator acting on \mathbf{r}' , and the density function $v \in H^{\frac{1}{2}}(\partial\Omega)$ is the boundary data. For a discussion on direct and indirect boundary integral equations see [35, Chapter 1]. The problem setting is illustrated in Figure 1 (left).

Remark 1. The boundary $\partial\Omega$ often matches the magnet poles or the vacuum chamber while particle beams with *large acceptance* may occupy most of the available space. Bringing the sensor close to the boundary is a non-trivial task and dedicated measurement equipment needs to be designed. We will therefore focus on the inference of the boundary data v from measurements within the domain Ω . This has the disadvantage that the inverse source problem is ill-conditioned. The Bayesian framework is used in Section 5 to derive a regularization technique based on a prior field solution.

One benefit of the field representation by v is that a magnetic vector potential \mathbf{A} , defined via $\mathbf{B} = \operatorname{curl} \mathbf{A}$, is accessible by means of the vectorial single-layer potential \tilde{V} acting on the surface current density $\mathbf{s} := -\mathbf{n} \times \operatorname{grad}_{\mathbf{r}'} v$,

$$\mathbf{A} = \mu_0 \int_{\partial\Omega} u^*(\mathbf{r}, \mathbf{r}') \mathbf{s}(\mathbf{r}') d\mathbf{r}' := (\tilde{V}\mathbf{s})(\mathbf{r}). \quad (2.4)$$

This follows from the definition of the magnetic vector potential and the equivalence of the double layer and eddy ring [28].

Remark 2. Although the boundary data v in the indirect representation formula is fictitious, evaluating (2.3) always yields an exact magneto-static solution, i.e., (2.1) holds in Ω for \mathbf{B} and \mathbf{H} (see [35, Section 1.1]).

2.1 Discretization

In boundary-element methods (BEM), the boundary data is approximated by locally supported basis functions on a boundary mesh. The algorithms presented in this paper have been implemented in C++ using the Boundary Element Based Engineering Library (BEMBEL) [7]. This enables a discretization of $\partial\Omega$ by means of non-uniform rational basis spline (NURBS) parameterizations as proposed in [9]. NURBS parameterizations are commonly used in computer-aided design and enable the exact representation of a large class of geometries. For an isogeometric approach the boundary data v is approximated in the finite-dimensional space $\mathcal{V}_h \subset H^{\frac{1}{2}}(\partial\Omega)$, which is spanned by patchwise tensor product basis-splines of degree p (see for example [3]). This yields the approximated boundary data v_h and surface current density \mathbf{s}_h in terms of the N degrees of freedom v_k . A tensor product basis-spline of degree $p = 3$ is shown in Figure 1 (right), together with the resulting surface current density for some given v over sixteen elements. In the following, the vector of degrees of freedom for the discretized double-layer potential will be denoted as the *state vector* $\mathbf{v} = (v_1, \dots, v_N)^T \in \mathbb{R}^N$.

The normal component of the magnetic flux density $\mathbf{n} \cdot \mathbf{B}$ is proportional to the Neumann trace, i.e., $\mathbf{n} \cdot \mathbf{B} = -\mu_0 \mathbf{n} \cdot \operatorname{grad} \phi_m$, where $\mu_0 = 4\pi \cdot 10^{-7}$ Vs/Am is the vacuum permeability. For Lipschitz domains this holds almost everywhere on $\partial\Omega$.

The component $\mathbf{n} \cdot \mathbf{B}$ provides the Neumann data for the computation of the state vector \mathbf{v} . To this end, we apply the Neumann trace operator to the double layer potential in (2.3), which results in the *hypersingular integral operator*, denoted as $D : H^{\frac{1}{2}}(\partial\Omega) \rightarrow H^{-\frac{1}{2}}(\partial\Omega)$ (see [35, p. 6]). Following a Galerkin discretization scheme

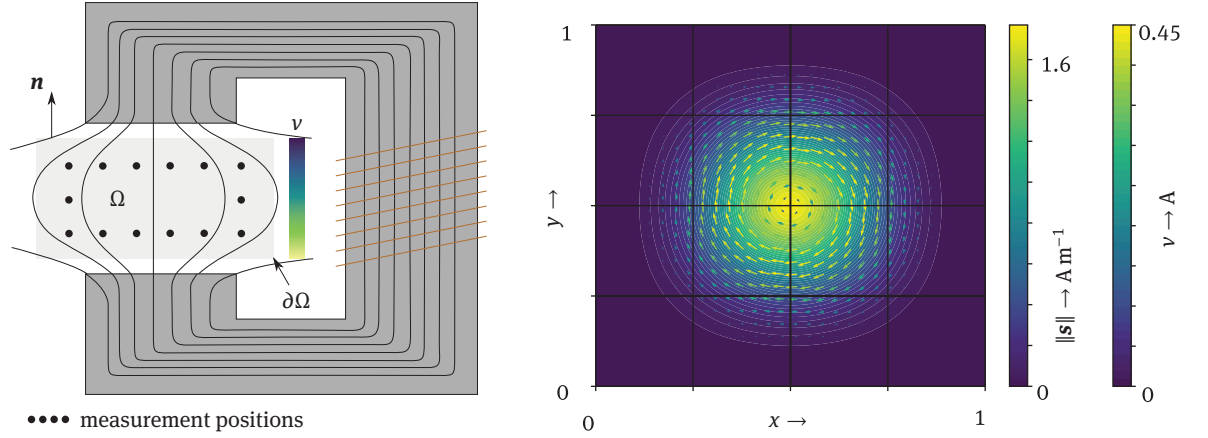


Figure 1: Left: A domain Ω , its boundary $\partial\Omega$ and the outward directed unit vector \mathbf{n} in the air gap of an electromagnet. Right: A tensor product basis spline of degree $p = 3$, defined over sixteen square elements. The vector field illustrates the resulting surface current density \mathbf{s} .

for D , we derive the linear equation system

$$D\mathbf{v} = \mathbf{f}, \quad (2.5)$$

where

$$[D]_{k,l} = -\mu_0 \langle \varphi_k, (D\varphi_l) \rangle_{\partial\Omega} + \langle \varphi_k, \varphi_l \rangle_{\partial\Omega} \quad \text{and} \quad [\mathbf{f}]_k = \langle \varphi_k, \mathbf{n} \cdot \mathbf{B} \rangle_{\partial\Omega}. \quad (2.6)$$

The k -th tensor product basis-splines is denoted by φ_k . The explicit definition of these functions in the isogeometric framework is given in [3]. Practically we use the representation

$$\langle \varphi_k, (D\varphi_l) \rangle_{\partial\Omega} = \frac{1}{4\pi} \int_{\partial\Omega} \int_{\partial\Omega} \frac{\mathbf{curl}_{\partial\Omega} \varphi_k(\mathbf{r}) \cdot \mathbf{curl}_{\partial\Omega} \varphi_l(\mathbf{r}')}{|\mathbf{r} - \mathbf{r}'|} d\mathbf{r} d\mathbf{r}', \quad (2.7)$$

where

$$\mathbf{curl}_{\partial\Omega} \varphi(\mathbf{r}) = \mathbf{n}(\mathbf{r}) \times \text{grad}_{\mathbf{r}} \tilde{\varphi}(\mathbf{r}) \quad \text{for } \mathbf{r} \in \partial\Omega \quad (2.8)$$

is the vectorial surface curl and $\tilde{\varphi}$ is extending φ locally into the neighborhood of $\partial\Omega$ (see [35, Section 1.1]).

The regularization term $\langle \varphi_k, \varphi_l \rangle_{\partial\Omega}$ is introduced as a cure to the null space of D (see [35]) such that $[D]_{k,l}$ is positive definite.

Remark 3. In many applications, a magnet simulation based on the finite element method (FEM) provides a low order approximation of \mathbf{B} in the vacuum chamber. Low order FEM approximations are not useful for particle tracking (see for instance the discussions in [15] and [2]), but they can be used to evaluate the Neumann data $\mathbf{n} \cdot \mathbf{B}$ on the domain boundary to compute the state vector \mathbf{v} . We can then use (2.4) for the smooth evaluation of the magnetic vector potential in the vicinity of the particle beam. Similar approaches have been developed for the efficient, but accurate force calculation in electrical machines [31].

Remark 4. Given a low order FEM solution, we can evaluate \mathbf{B} on a point cloud in the vicinity of the domain boundary. From this point cloud, the normal component $\mathbf{n} \cdot \mathbf{B}$ can be evaluated by linear interpolation. The accuracy of this interpolation can be controlled by the resolution of the point cloud, and it is limited by the accuracy of the finite element solution.

We can derive an equation for the evaluation of \mathbf{B} at the position \mathbf{r} , by taking the curl of (2.4)

$$\mathbf{B}(\mathbf{r}, \mathbf{v}) = -\mu_0 \text{curl} \sum_{n=1}^N v_n \int_{\partial\Omega} u^*(\mathbf{r}, \mathbf{r}') \mathbf{curl}_{\partial\Omega} \varphi_n(\mathbf{r}') d\mathbf{r}', \quad (2.9)$$

where φ_n is the n -th tensor product basis spline on the boundary mesh.

The Aubin–Nitsche formalism allows to derive point-wise error estimates for the evaluation of the discretized boundary integral equations (see [45, Theorem 12.8], [38, Example 4.2.15]). As it will be relevant for the upcoming discussions, we provide the result for the indirect Neumann problem in Theorem 1.

Theorem 1. *For the solution of the Neumann problem, using the indirect double-layer potential, and assuming a sufficiently smooth boundary, there holds the point-wise estimate [9, Theorem 7.1]*

$$|(Wv)(\mathbf{r}) - (Wv_h)(\mathbf{r})| \leq c(\mathbf{r})h^{2p+1}, \quad \mathbf{r} \in \Omega, \quad (2.10)$$

where v_h is the approximated stream function using B-splines of polynomial degree p , and h is a mesh parameter, which is often identified with the maximum edge length of all boundary elements.

The constant $c(\mathbf{r})$ decreases rapidly with increasing distance of \mathbf{r} to the boundary. This is known as the *smoothing property* in boundary element methods.

2.2 A Local Expansion for Particle Tracking

In particle beam dynamics the motion of a relativistic particle is usually expressed in so called phase-space coordinates. The momentum variables in phase-space coordinates are more abstract and differ from the ones used in classical mechanics, but this has the advantage that certain invariants of motion are conserved for a passage of the particle through a static magnetic field (see [47, Chapter 2]).

From the Euler–Lagrange formalism, the equations of motion result in Hamilton’s equations

$$\frac{d\mathbf{q}}{dt} = \frac{\partial H}{\partial \mathbf{p}}, \quad \frac{d\mathbf{p}}{dt} = -\frac{\partial H}{\partial \mathbf{q}}, \quad (2.11)$$

where $\mathbf{z} := (\mathbf{q}^T, \mathbf{p}^T)^T$ expresses the phase space coordinates, with \mathbf{q} denoting the particles coordinate vector and \mathbf{p} its canonical momentum. In the absence an electric field the Hamiltonian H is defined as

$$H := c\sqrt{(\mathbf{p} - q\mathbf{A})^2 + m^2 c^2}, \quad (2.12)$$

where c denotes the velocity of light, q the particle charge and m its mass. Hamilton’s equations (2.11) may be formulated as an ordinary differential equation system of the type

$$\frac{d}{dt}\mathbf{z} = \mathbf{f}(t, \mathbf{z}). \quad (2.13)$$

Its solution by numerical integration for a given initial condition is the main objective of single particle tracking.¹

Due to the partial derivatives $\frac{\partial H}{\partial \mathbf{q}}$, the spatial derivatives of the magnetic vector potential $\partial_i A_j$ for $i, j \in x, y, z$ are involved on the right-hand side of (2.13). A useful field model must therefore provide \mathbf{A} , as well as its spatial derivatives of first order. Approaches for numerical integration of (2.13) may use explicit or implicit higher order Runge–Kutta schemes [19] or also Lie-algebraic methods [48].

In principle one could apply the representation formula (2.4) directly in the numerical integration scheme. The spatial derivatives can be computed by differentiating the Green’s function u^* analytically and evaluating the resulting integral equation numerically. This, however, requires the repeated integration over the whole boundary $\partial\Omega$ for each particle at each position, which is not known a-priori.

More efficient approaches have been proposed, using local expansions of the magnetic vector potential around a reference trajectory by either Taylor approximations [11] or the fitting of \mathbf{A} by solid harmonic functions within intercepting spheres [2].

Using Taylor expansions makes it necessary to impose (2.1) to recover a magneto-static solution. This is implied by using the solid harmonic functions. We therefore follow the approach developed in [2], but in contrast to fitting \mathbf{A} on the surfaces of spheres, we make use of a local expansion of the Green’s function according to Theorem 2 for the computation of the local harmonic expansion. This allows us to derive analytical bounds for the truncation errors and also the fast calculation of the local expansion for an ensemble of state vectors.

¹ Usually one performs a change of coordinates to obtain a formulation in terms of the path length as the independent variable.

Theorem 2 ([29, Section 3.4]). Consider a point $\mathbf{r}_0 \in \mathbb{R}^3$ and the two difference vectors $\mathbf{r} - \mathbf{r}_0 = (r, \theta, \varphi)$ and $\mathbf{r}' - \mathbf{r}_0 = (r', \theta', \varphi')$, given in spherical coordinates. For $r < r'$, the expansion of the Green's function is

$$u^*(\mathbf{r}, \mathbf{r}') \approx \frac{1}{4\pi\|\mathbf{r} - \mathbf{r}'\|} = \frac{1}{4\pi} \sum_{l=0}^{\infty} \sum_{m=-l}^l \frac{1}{2l+1} \frac{r^l}{r'^{l+1}} Y_l^m(\theta, \varphi) Y_l^m(\theta', \varphi')^*, \quad (2.14)$$

where $Y_l^m : \mathbb{R}^2 \rightarrow \mathbb{C}$ is the spherical harmonic function of order l and degree m , and $(\cdot)^*$ denotes the complex conjugate.

The functions $r^l Y_l^m$ and Y_l^m/r'^{l+1} are the regular and irregular solid harmonic functions, which are eigensolutions of the Laplace equation.

By Theorem 2, the magnetic vector potential may be expanded at the position \mathbf{r}_j , according to

$$\mathbf{A}(\mathbf{r}) \approx \mathbf{A}_L(\mathbf{r}) := \sum_{l=0}^L \sum_{m=-l}^l \mathbf{m}_l^m(\mathbf{r}_j) r^l Y_l^m(\theta, \varphi) \quad \text{with } \|\mathbf{r} - \mathbf{r}_j\| < \min_{\mathbf{r}' \in \partial\Omega} \|\mathbf{r}' - \mathbf{r}_j\|. \quad (2.15)$$

This expansion is valid inside the largest sphere with center \mathbf{r}_j , which does not enclose any part of the domain boundary.

The evaluation position $\mathbf{r} - \mathbf{r}_j$ is expressed in spherical coordinates (r, θ, φ) and the moments $\mathbf{m}_l^m(\mathbf{r}_j)$ are given by

$$\mathbf{m}_l^m(\mathbf{r}_j) := \mu_0 \frac{1}{2l+1} \int_{\partial\Omega} \mathbf{s}(\mathbf{r}') \frac{Y_l^m(\theta', \varphi')^*}{r'^{l+1}} d\mathbf{r}', \quad (2.16)$$

where $\mathbf{r}' - \mathbf{r}_j = (r', \theta', \varphi')$. It is possible to assemble the integral (2.16) for the basis functions used for the approximation of \mathbf{v}_h . In this way, the moments can be evaluated rapidly by matrix vector products for an ensemble of state vectors.

The moments $\mathbf{m}_l^m(\mathbf{r}_j)$ can be computed for J points \mathbf{r}_j along a reference trajectory. The particle tracking can then be performed on (2.15) and it requires only the evaluations of the solid harmonics $r^l Y_l^m(\theta, \varphi)$. As the solid harmonics are eigensolutions of the Laplace equation, evaluating the truncated sum in (2.15) yields an exact magneto-static solution.

Remark 5. The approach based on Theorem 2 can also be applied to other field representations based on integral formulations, such as BEM-FEM coupling or volume integral methods.

Theorem 3. The error in the truncation \mathbf{A}_L is bounded by

$$|\mathbf{A}(\mathbf{r}) - \mathbf{A}_L(\mathbf{r})| \leq \frac{\mathbf{C}}{R-r} \left(\frac{r}{R}\right)^L$$

with

$$\mathbf{C} := \frac{\mu_0}{4\pi} \int_{\partial\Omega} |\mathbf{s}(\mathbf{r}')| d\mathbf{r}', \quad (2.17)$$

where $R := \min_{\mathbf{r}' \in \partial\Omega} \|\mathbf{r}' - \mathbf{r}_j\|$ and $r < R$.

Proof. The truncation error is given by the coefficients $l \geq L+1$. From the addition theorem of the spherical harmonic functions (see [50, equation (14.30.9)]) we deduce that

$$\left| \frac{4\pi}{2l+1} \sum_{m=-l}^l Y_l^m(\theta', \varphi')^* Y_l^m(\theta, \varphi) \right| \leq 1.$$

Moreover, with $r' \leq R$ for all $\mathbf{r}' \in \partial\Omega$ and the triangle inequality we find that

$$|\mathbf{A}(\mathbf{r}) - \mathbf{A}_L(\mathbf{r})| \leq \mathbf{C} \sum_{l=L+1}^{\infty} \frac{r^l}{R^{l+1}} = \frac{\mathbf{C}}{R-r} \left(\frac{r}{R}\right)^L$$

with \mathbf{C} according to (2.17). In the last equation we have used the closed form of the geometric series

$$\sum_{l=L+1}^{\infty} c^{l+1} = \frac{c^{L+1}}{1-c}$$

for $|c| < 1$. □

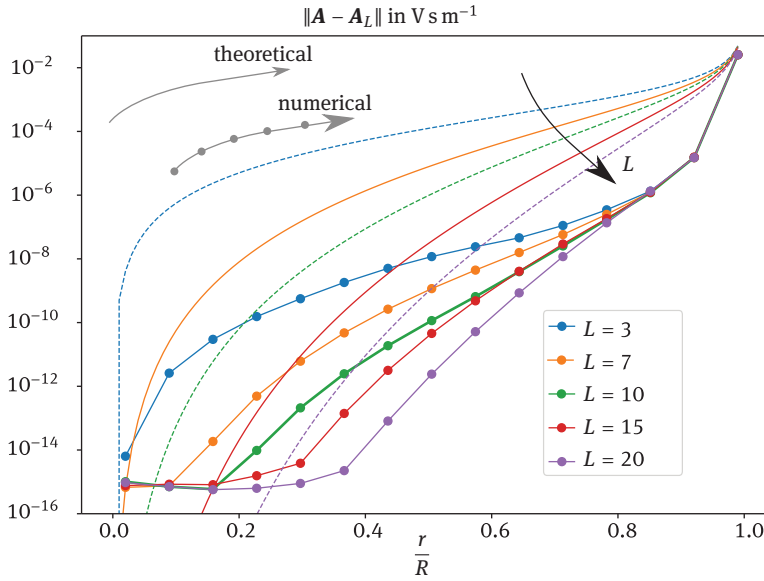


Figure 2: Truncation error for the evaluation of the magnetic vector potential over the ratio r/R . Dashed: Theoretical bound. Solid: Observed error in a numerical experiment.

The truncation error for the evaluation of \mathbf{A} in Ω can be controlled by means of the truncation parameter L as well as the number of expansion positions J . This is conceptually equivalent to p and h refinement in boundary and finite element methods.

Figure 2 shows the theoretical bounds for the truncation error as a function of the ratio $\frac{r}{R}$ and also the truncation errors observed in a numerical experiment. The rates of the theoretical bounds meet our observations, but the absolute values are pessimistic. However, this is uncritical, since the truncation error $|\mathbf{A}(\mathbf{r}) - \mathbf{A}_L(\mathbf{r})|$ can be computed for a given L . In this way L can be adjusted for an adaptive expansion.

3 The Hall Probe Mapper System

The Hall probe mapper system is shown in Figure 3 (left). It uses the stages of a coordinate measuring machine (CMM) to manipulate the position of a three-axes Hall sensor in the magnetic field. The system allows for a distance triggered acquisition of the Hall voltages during the stage movement. This improves the required measurement duration compared to measurements in start-stop mode, but also causes the mapper arm to vibrate due to perturbations of the stage motion in the μm range.

A mathematical model for three axes Hall probe measurements is now derived. This mathematical model is coupled with the boundary integral equation for the magnetic flux density \mathbf{B} , which yields the so-called observation operator $\mathbf{H} : \mathbf{v} \mapsto \hat{\mathbf{y}}$. It maps a state vector \mathbf{v} to a *predicted measurement vector* $\hat{\mathbf{y}}$. Finally, a realistic noise model will be derived, which includes the impact of positioning perturbations due to mapper-arm vibrations.

3.1 The Observation Operator

The voltages measured by Hall sensors can have complicated dependencies on the three components of the magnetic flux density. These stem from planar Hall effects and geometric imperfections, but also from non-linearity errors of the sensor transfer function. Calibration techniques allow for the characterization of planar and axial Hall effects by rotating the sensor in a reference field. This gives rise to the sensitivity function

$$s_i(\mathbf{B}) = \sum_{l=0}^L \sum_{m=-l}^l c_i^{l,m} |\mathbf{B}|^l Y_l^m(\theta(\mathbf{B}), \varphi(\mathbf{B})), \quad (3.1)$$

with the complex calibration coefficients $c_i^{l,m} \in \mathbb{C}$, where $c_i^{l,m} = -(c_i^{l,-m})^*$, and the spherical harmonic functions Y_l^m . The angles $\theta(\mathbf{B})$ and $\varphi(\mathbf{B})$ denote the polar and azimuth angles of the \mathbf{B} field in a sensor coordinate system (see Figure 3 (a)). We have introduced the index $i \in \{0, 1, 2\}$ to distinguish the three Hall sensors involved in a three component measurement. The sensors do not need to be aligned with any of the magnet coordinate axes. Their misalignment is encoded in the coefficients $c_i^{l,m}$. Moreover, the three sensors cannot be mounted at exactly the same spot. For this reason, the positions of the three Hall sensors are denoted by $\mathbf{r}_m + \mathbf{o}_i$, where \mathbf{r}_m is a measurement position (usually the position measured by the linear encoders) and the vectors \mathbf{o}_i denote the displacements of the Hall sensors with respect to this position. Typically, the displacements between the sensors are in the mm range. The absolute sensor position and orientation can be identified by measurements in calibration magnets and is therefore assumed to be given.

Remark 6. In case of a linear Hall sensor, the sensitivity function s_i may be expressed by means of the orientation vector \mathbf{n}_i , and the zero field offset voltage $U_{0,i}$ such that $s_i(\mathbf{B}) = \mathbf{n}_i \cdot \mathbf{B} + U_{0,i}$. In this case all coefficients with $l > 1$ vanish in (3.1). Whereas the offset voltage $U_{0,i}$ is encoded in the $l = 0$ term, the projection $\mathbf{n}_i \cdot \mathbf{B}$ is encoded in the terms $c_i^{1,m} |B| Y_1^m$.

To establish the observation operator, we define the three Hall voltages by

$$U_i(\mathbf{r}_m) := s_i(\mathbf{B}(\mathbf{r}_m + \mathbf{o}_i)), \quad i \in \{0, 1, 2\}, \quad (3.2)$$

and sort the measurement vector according to the scheme $\tilde{\mathbf{y}} = (U_0(\mathbf{r}_1), \dots, U_0(\mathbf{r}_M), U_1(\mathbf{r}_1), \dots, U_2(\mathbf{r}_1), \dots)^T$, considering M measurement positions. The m -th row of the observation operator $\mathbf{H} : \mathbb{R}^N \rightarrow \mathbb{R}^{3M \times N}$ is computed by

$$[\mathbf{H}(\mathbf{v})]_{m+iM} = s_i(\mathbf{B}(\mathbf{r}_m + \mathbf{o}_i, \mathbf{v})) \quad (3.3)$$

for $i \in \{0, 1, 2\}$ and $\mathbf{B}(\mathbf{r}, \mathbf{v})$ according to (2.9).

Remark 7. One benefit of the indirect double layer potential formulation is that the observation operator imposes a magneto-static solution without the necessity to solve a linear equation system. To see this, we consider, as an alternative, a field model based on a finite element approximation. The coefficients $\mathbf{x} \in \mathbb{R}^N$ of this approximation are related to the boundary data \mathbf{b} by means of a linear equation system $\mathbf{A}\mathbf{x} = \mathbf{P}\mathbf{b}$, where \mathbf{A} is a sparse Galerkin matrix and $\mathbf{P} : \mathbf{b} \mapsto \mathbf{x}$ is a sparse extension operator (see [12]). The observation operator for measurements within the domain needs to be constructed on the approximation space. We denote this evaluation operation by the matrix \mathbf{S} . In case of a linear sensor, it therefore follows the observation operator $\mathbf{H} = \mathbf{S}\mathbf{A}^{-1}\mathbf{P}$ (see [21]). Due to the sparsity of \mathbf{A} it is usually much more effective, to solve this equation for multiple right-hand sides than performing a direct inversion. Whenever the right-hand side \mathbf{b} changes, the solution of a sparse linear equation system of size $N \times N$ is required to evaluate the measurement operation.

3.2 The Noise Model

For the uncertainty quantification, a noise model is needed which represents the real measurement data. We therefore follow the guide to the expression of uncertainty in measurement (GUM) [49]. It proposes to introduce input quantities to the measurement equation (3.3), in order to model the relevant physical phenomena, which are perturbing the measurements. Then, the uncertainty in the measurands is quantified by means of a first order Taylor approximation of the measurement equation with respect to the input quantities. This procedure is justified as long as the values of the input quantities are small deviations from zero.

In case of the Hall probe mapper system, the measurements are mostly affected by perturbations of the sensor position and orientation, due to the vibration of the mapper arm. We therefore include five degrees of freedom for each measurement position as input quantities. Three displacements, denoted as w_x , w_y and w_z , and two rotations φ_x and φ_y . The input quantities are illustrated in Figure 3. All input quantities are collected into the $5M$ -dimensional vector of mechanical perturbations \mathbf{d} .

² A third possible rotation is neglected as no axial rotation has been observed for the Hall probe mapper system.

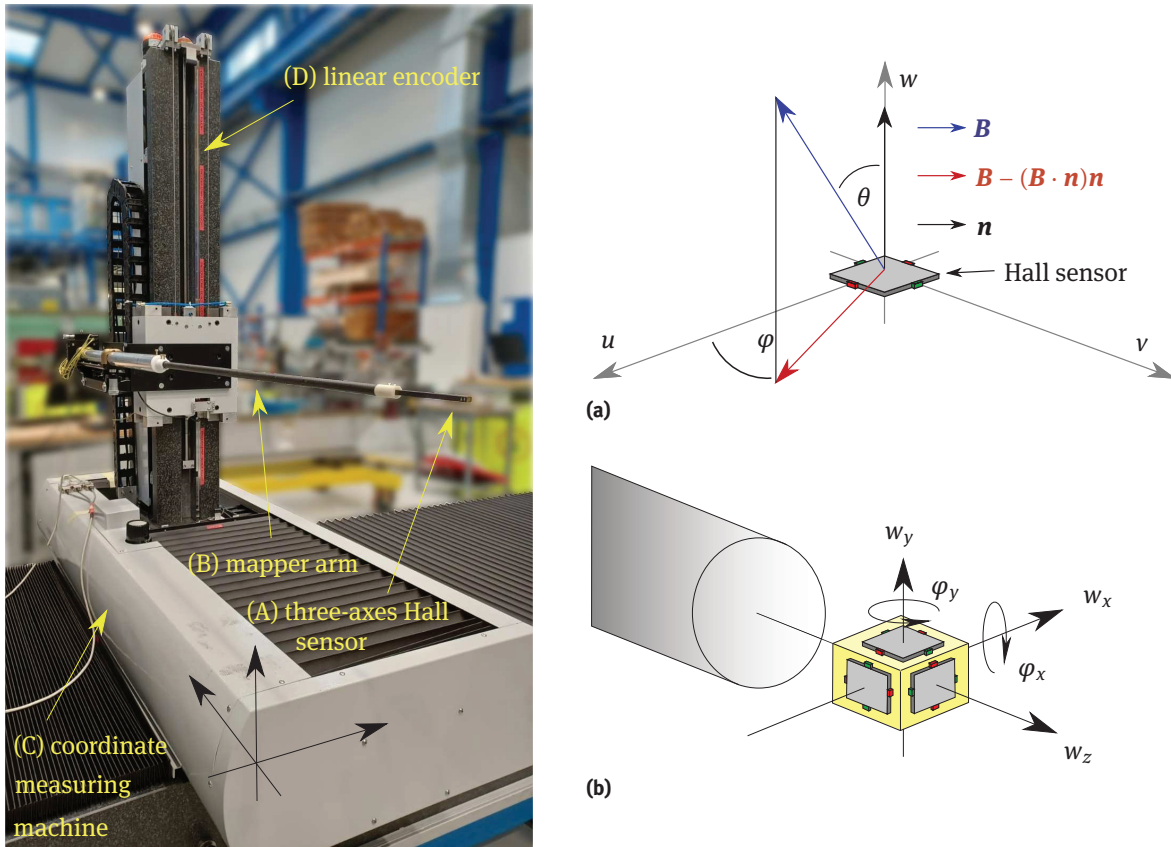


Figure 3: Left: The Hall probe mapper system. It uses the stages of a coordinate measuring machine (C) to manipulate the position of a three axes Hall sensor (A) within an accelerator magnet. The sensor is mounted on an arm (B). The stage position is measured by linear encoders (D). Right: (a) A Hall sensor and a local coordinate system (u, v, w) . The angles θ and φ are the polar and azimuth angles in the (u, v, w) coordinates. (b) Input quantities for modeling the mechanical perturbations of the sensor position. These perturbations occur due to position errors and arm vibrations.

The mechanical perturbations are caused by random perturbations of the stage motion and are therefore not deterministic. However, the vibrations of the mapper arm lead to correlations between the measuring positions. These correlations have been determined by optical measurements in the machine setup. This yields a statistical model for the mechanical perturbations, which is of the type $\mathbf{d} \sim \mathcal{N}(\mathbf{0}, \Sigma_{\mathbf{d}})$, with a covariance matrix $\Sigma_{\mathbf{d}}$.

As proposed in the GUM, the impact on the measurement vector \mathbf{y} is determined by means of a first order Taylor approximation. To this end, we introduce the rotation matrix $\mathbf{M}(\varphi_x, \varphi_y) \in \mathbb{R}^{3 \times 3}$, which describes the rotations around the transversal axis³. We then substitute $\mathbf{B} \mapsto \mathbf{M}(\varphi_x, \varphi_y) \cdot \mathbf{B}$ and $\mathbf{o}_i \mapsto \mathbf{o}_i + (w_x, w_y, w_z)^T$ in (3.3) and derive the resulting expressions with respect to the input parameters w_x, w_y, w_z, φ_x and φ_y . This yields the five sensitivity matrices $\partial \mathbf{H}_j \in \mathbb{R}^{M \times N}$ for $j \in \{w_x, w_y, w_z, \varphi_x, \varphi_y\}$. Collecting the vectors $\partial \mathbf{H}_j \mathbf{v}$ in the matrix $\partial \mathbf{H}(\mathbf{v}) = (\text{diag}(\partial \mathbf{H}_{w_x} \mathbf{v}), \dots, \text{diag}(\partial \mathbf{H}_{\varphi_y} \mathbf{v})) \in \mathbb{R}^{M \times 5M}$, the Taylor approximation can be denoted by

$$\tilde{\mathbf{y}} \approx \mathbf{H}(\mathbf{v}) + \partial \mathbf{H}(\mathbf{v}) \mathbf{d}. \quad (3.4)$$

The matrices $\partial \mathbf{H}_j$ are fully populated and might occupy a large memory. For the estimation of the measurement noise, the computation of the products $\partial \mathbf{H}_j \mathbf{v}$ with an accuracy in the percent range is tolerable. To this end, the matrix vector products can be computed on low rank approximation saving a considerable amount of memory. In this context fast multipole methods are particularly effective, since all five matrix vector products are using the same upward and downward pass operations [17].

³ Assuming without loss of generality that the mapper arm is aligned with respect to the z -axis.

Proposition 1. *With the Gaussian model for the mechanical perturbations $\mathbf{d} \sim \mathcal{N}(\mathbf{0}, \Sigma_{\mathbf{d}})$, a Gaussian model for the electronic noise $\mathbf{y} \sim \mathcal{N}(\bar{\mathbf{y}}, \Sigma_{\mathbf{y}})$ and a given state vector \mathbf{v} , the noise model is given by*

$$\mathbf{y} \sim \mathcal{N}(\bar{\mathbf{y}}, \mathbf{R}(\mathbf{v})) = \mathcal{N}\left(\bar{\mathbf{y}}, \overbrace{\frac{\partial \mathbf{H}(\mathbf{v}) \Sigma_{\mathbf{d}} \partial \mathbf{H}(\mathbf{v})^T}{\text{mechanical noise}} + \frac{\Sigma_{\mathbf{y}}}{\text{electronic noise}}}^{=: \mathbf{R}(\mathbf{v})}\right). \quad (3.5)$$

Proof. The electronic noise is assumed to be additive, such that $\mathbf{y} = \bar{\mathbf{y}} + \boldsymbol{\epsilon}_{\mathbf{y}}$, with $\boldsymbol{\epsilon}_{\mathbf{y}} \sim \mathcal{N}(\mathbf{0}, \Sigma_{\mathbf{y}})$, and uncorrelated to \mathbf{d} , this means $E(\boldsymbol{\epsilon}_{\mathbf{y}} \mathbf{d}^T) = 0$. It follows from the linearity of the expected value function that $E(\mathbf{y}) = \mathbf{H}(\mathbf{v})$, and

$$\begin{aligned} E((\mathbf{y} - E(\mathbf{y}))(\mathbf{y} - E(\mathbf{y}))^T) &= E(\mathbf{y}\mathbf{y}^T) - E(\mathbf{y})E(\mathbf{y})^T \\ &= E((\mathbf{H}(\mathbf{v}) + \partial \mathbf{H}(\mathbf{v})\mathbf{d} + \boldsymbol{\epsilon}_{\mathbf{y}})(\mathbf{H}(\mathbf{v}) + \partial \mathbf{H}(\mathbf{v})\mathbf{d} + \boldsymbol{\epsilon}_{\mathbf{y}})^T) - (\mathbf{H}(\mathbf{v}))(\mathbf{H}(\mathbf{v}))^T \\ &= \partial \mathbf{H}(\mathbf{v})E(\mathbf{d}\mathbf{d}^T)\partial \mathbf{H}(\mathbf{v})^T + E(\boldsymbol{\epsilon}_{\mathbf{y}}\boldsymbol{\epsilon}_{\mathbf{y}}^T) = \partial \mathbf{H}(\mathbf{v})\Sigma_{\mathbf{d}}\partial \mathbf{H}(\mathbf{v})^T + \Sigma_{\mathbf{y}}. \quad \square \end{aligned}$$

Remark 8. Both covariance matrices for mechanical and electronic noise, $\Sigma_{\mathbf{d}}$ and $\Sigma_{\mathbf{y}}$ have been estimated from measurement data in the characterization phase of the Hall probe mapper system. Whereas optical measurements of the mapper arm were used to estimate $\Sigma_{\mathbf{d}}$, the signal noise covariance $\Sigma_{\mathbf{y}}$ was estimated from measurements in a zero Gauss chamber, insulating the probe from external fields. It was found that covariances in the electronic noise are negligible for sampling frequencies in the 10 – 100 Hz range. This implies that the electronic noise can be modeled by means of a diagonal covariance matrix $\Sigma_{\mathbf{y}}$. The matrix $\Sigma_{\mathbf{d}}$ is sparse, as correlations between mapper moves can be neglected.

4 Magnetic Measurements and the Prior Field Solution

It is possible to obtain the boundary data from a numerical field simulation. This procedure was described in detail in Section 2. The following section aims at deriving a hybrid model, that combines the first principle modeling (see Section 2) with data driven modeling, based on measurements [25]. In this context, it is important to consider the measurement uncertainties described in the previous section.

The inference of boundary data from measurements leads to the concept of Bayesian inference. Before going into detail, we will give an example for the practical application of our approach. The theoretical considerations of the next section are applied to this practical example.

We consider the problem of determining the field quality in a curved dipole magnet, shown in Figure 4 (left). It is a spare magnet for in the Extra Low ENergy Antiproton ring (ELENA) [32]. The design of these magnets was associated with several challenges due to the low working range in terms of magnetic flux density in the iron yoke, also the tough field quality requirements in combination with a small bending radius of only ~ 1 m [39].

We consider a curved domain of interest Ω , which is covering the magnet's air gap and fringe field region. This domain is shown in Figure 4 (right) together with a boundary mesh used for the numerical approximation. Some parameters related to the domain of interest can be found in Table 1.

A numerical field simulation of the magnet is available by means of a lowest order finite element solution using the software Opera 3D and it is used to construct a *prior* BEM approximation. We will see in Section 5 how this field solution can be incorporated as a prior for the hybrid model.

Magnet Parameters					
Min/Max Gap Height	Pole Width	Mean Radius of Curvature	Bending Angle	Good Field Region ($x \times y$)	
75/76 mm	200 mm	0.927 m	60 deg	44 × 66 mm	
Boundary Parameters					
Height	Width	Length (z)	Number of Elements	Number of DoFs	
70 mm	200 mm	1680 mm	8576	13402	

Table 1: Geometric parameters of the magnet and the domain of interest.

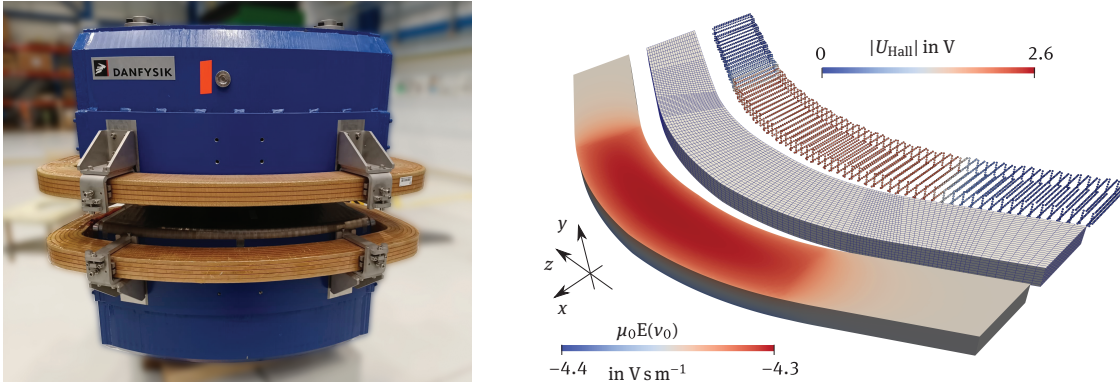


Figure 4: Left: The ELENA bending dipole magnet. Right: The measurement data U_{Hall} as a point cloud, the boundary mesh as well as the mean of the prior boundary data $\mu_0 E(v_0)$, determined from a numerical field simulation.

We make use of the approach discussed in Remark 4 and perform h, p -refinement until the difference in $\mathbf{n} \cdot \mathbf{B}$, between the FEM and BEM solution converges to 2 units in 10 000. The resulting approximation space requires $N = 13\,402$ cubic ($p = 3$) basis-splines on an irregular mesh, with increased resolution in the fringe fields, where the field decays most rapidly. The boundary mesh was constructed manually using the NURBS package in Octave [44]. It is shown as a contour plot in Figure 4 (right).

Remark 9. It should be noted that the role of the FEM solution is to provide an initial guess for the Neumann data and its smoothness in the fringe field region. As it is the case for the magnet under consideration, standard tools for magnet design use low-order finite element methods, with a considerably lower convergence compared to a higher-order BEM formulation. Approximation errors in the process of fitting the Neumann data are negligible with respect to the engineering bias due to manufacturing tolerances, as well as uncertainties in geometric and material properties (see Figure 8 (left)). This engineering bias must be corrected by magnetic measurements.

The Hall probe mapper system is configured to sample the field along the domain boundary. Due to the thickness of the supporting structure and also the sensor housing, it is not possible to sample the $\mathbf{n} \cdot \mathbf{B}$ component at the boundary $\partial\Omega$ directly. For this reason the system is sampling the field along the boundary of a smaller domain, inscribed in Ω . We denote this measurement domain by Ω_M .

At this point we need to be careful not to distribute measurements too close to the boundary $\partial\Omega$. This is due to the fact that even if we consider an exact numerical integration, the constant $c(\mathbf{r})$ in Theorem 1 approaches infinity for the limit $\|\mathbf{r} - \mathbf{r}'\| \rightarrow 0$, $\mathbf{r}' \in \partial\Omega$.

The absolute values for the approximation error depend on the smoothness of the solution and cannot be determined a priori. A-posteriori error estimates for boundary element methods are found in [26]. As we are generating a boundary mesh based on a given FEM approximation, the approximation errors can be estimated by computing the difference between the BEM and FEM solutions in the vicinity of the boundary. In the example presented in this work, approximation errors are found to fall below 2 units in 10 000, within a distance of 8 mm. For this reason, the mapper system is set up to maintain this distance for all measurements.

We can exploit the physical relations imposed by the field model and place measurements only at the boundary of the measurement domain Ω_M . In this way, we need $\mathcal{O}(1/h_{\text{meas}}^2)$ measurement positions, to achieve a resolution h_{meas} . To further increase efficiency, we acquire the Hall voltages on-the-fly, as the stages of the mapper system move. In this way the measurement duration scales linearly with respect to the desired measurement resolution $\mathcal{O}(1/h_{\text{meas}})$, as measurements along the scanning direction are fast. However, this also causes the mapper arm to vibrate, due to small imperfections in the stage motion. For the uncertainty quantification it is therefore crucial to consider the noise model we have developed in Section 3.2. The resulting move sequence is shown in Figure 5.

The Hall probe mapper is equipped with a calibrated three axes Hall sensor, hosting an electronic board for signal conditioning. We are therefore working with a linear model for the sensitivity function s , with $L < 2$ in (3.1) (see Remark 6).

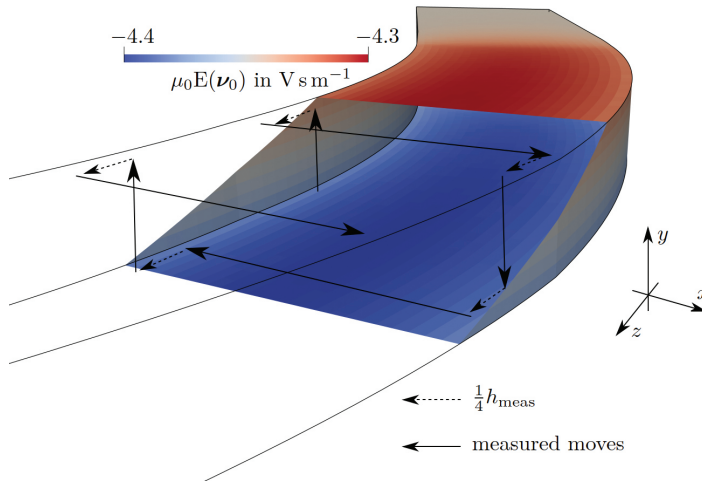


Figure 5: The measurement procedure. The Hall probe mapper is moving along the domain boundary in a rectangular spiral. Measurements are taken for all moves along the x and y axes. With a distance trigger to launch the acquisition of the Hall voltages, we obtain a point cloud of measurement positions. An example is shown in Figure 4 (right).

5 Measurement Postprocessing

In order to update our prior assumptions on the boundary data, which were obtained from the first principle modeling discussed in Section 2, we follow the Bayesian viewpoint where the state vector \mathbf{v} is considered as a random variable. In this way the uncertainty in \mathbf{v} can be interpreted by means of a probability density function (pdf) $p(\mathbf{v}) : \mathbb{R}^N \rightarrow \mathbb{R}$. This provides the mathematical framework to incorporate prior knowledge about the state vector \mathbf{v} and makes the practical application more flexible, since small and incomplete data sets leading to ill-posed inverse problems can be handled. In addition, the pdf $p(\mathbf{v})$ can be updated whenever new data becomes available. This establishes the basis for iterative learning schemes.

In the following, we denote by \mathbf{y} the vector of the measurement data. To make the difference between the actual measurement data \mathbf{y} and the model prediction $\tilde{\mathbf{y}}$ apparent, we add a superscript tilde to the latter vector.

Central to Bayesian inference is Bayes' rule of probability

$$\underbrace{p(\mathbf{v}|\mathbf{y})}_{\text{posterior}} \propto \underbrace{p(\mathbf{y}|\mathbf{v})}_{\text{likelihood}} \underbrace{p(\mathbf{v})}_{\text{prior}}, \quad (5.1)$$

which states that the posterior pdf $p(\mathbf{v}|\mathbf{y})$ for \mathbf{v} , given the measurement data \mathbf{y} , is proportional to the product of the likelihood function $p(\mathbf{y}|\mathbf{v})$ and a prior pdf $p(\mathbf{v})$.

The likelihood function is derived by coupling the statistical model for the measurement noise with the numerical model for the measurement operation by means of the observation operator \mathbf{H} . A Gaussian noise model was derived explicitly for the Hall probe mapper system in Section 3. The likelihood function follows after substituting the observation operator $\mathbf{H}(\mathbf{v})$ for $\tilde{\mathbf{y}}$, and considering the result as a function of \mathbf{v} .

The impact of mechanical vibrations and positioning errors depends on the magnetic field, and therefore the state vector \mathbf{v} . This is encoded in the covariance matrix $\mathbf{R}(\mathbf{v})$. With the noise model according to (3.5), the sensor noise is Gaussian for a given \mathbf{v} . However, the posterior pdf $p(\mathbf{v}|\mathbf{y})$, is *not* a Gaussian distribution as \mathbf{R} depends on \mathbf{v} . One possibility to accommodate this has been presented in [25], where the mechanical perturbations \mathbf{d} have been considered as additional parameters. The posterior can then be split into Gaussian conditionals, and samples are drawn by Gibbs sampling.

In this work, we will make use of the prior state vector estimated from the numerical magnet simulation. The inference from measurement data aims to correct small differences in \mathbf{v} . This justifies estimating the noise covariance matrix \mathbf{R} with a prior for \mathbf{v} . Particularly we will use the expected value $E(\mathbf{v}_{j-1})$ to estimate the noise covariance matrix by $\mathbf{R}(E(\mathbf{v}_{j-1}))$, for the j -th Bayesian update. In this way we avoid the additional iteration over the mechanical perturbations \mathbf{d} , which yields a considerable reduction of computational complexity. In the

following, the resulting covariance matrix will be denoted by \mathbf{R} , neglecting the dependency on \mathbf{v} . However, the domains of validity of this simplification have so far not been determined explicitly and should be investigated in future research.

5.1 The Kálmán Filter

The update step of a linear Kálmán filter is derived from the posterior under the assumption of a linear observation operator \mathbf{H} and normal distributions for likelihood and prior. Denoting the prior pdf by $p(\mathbf{v}) \sim \mathcal{N}(\mathbf{v}_0, \mathbf{Q}_0)$, the posterior takes on the form $p(\mathbf{v}|\mathbf{y}) \sim \mathcal{N}(\mathbf{v}_1, \mathbf{Q}_1)$, with the posterior covariance matrix

$$\mathbf{Q}_1 = (\mathbf{H}^T \mathbf{R}^{-1} \mathbf{H} + \mathbf{Q}_0^{-1})^{-1} \quad (5.2)$$

and the expected value

$$\mathbf{Q}_1^{-1} \mathbf{v}_1 = \mathbf{H}^T \mathbf{R}^{-1} \mathbf{y} + \mathbf{Q}_0^{-1} \mathbf{v}_0. \quad (5.3)$$

A well-established alternative representation for \mathbf{v}_1 and \mathbf{Q}_1 is

$$\mathbf{Q}_1 = (\mathbf{I}_{N \times N} - \mathbf{K} \mathbf{H}) \mathbf{Q}_0, \quad (5.4)$$

$$\mathbf{v}_1 = \mathbf{v}_0 + \mathbf{K}(\mathbf{y} - \mathbf{H} \mathbf{v}_0), \quad (5.5)$$

where $\mathbf{I}_{N \times N} \in \mathbb{R}^{N \times N}$ is an identity matrix and $\mathbf{K} \in \mathbb{R}^{N \times N}$ is the *Kálmán gain*

$$\mathbf{K} := \mathbf{Q}_0 \mathbf{H}^T (\mathbf{H} \mathbf{Q}_0 \mathbf{H}^T + \mathbf{R})^{-1}. \quad (5.6)$$

This follows from the Sherman–Morrison–Woodbury formula [40].

Both formulations require a matrix inversion to compute the posterior covariance matrix \mathbf{Q}_1 . There are circumstances where this inversion is problematic. This for instance is the case in a high-dimensional setting, where \mathbf{H} can only be stored in a compressed format, such as a fast multipole matrix. Other compression possibilities would involve H/H2 matrices [9] or tensor decompositions [22]. Moreover, in some circumstances, the observation operator \mathbf{H} might require the inversion of a matrix itself (see Remark 7), although this is not the case for the indirect double-layer potential formulation according to (2.3). For these reasons it can be of advantage to use Theorem 4 to compute an ensemble of K state vectors \mathbf{v}_k and estimate the covariance matrix from these samples.

Theorem 4. *The solution \mathbf{v}_1^k of the linear equation system*

$$(\mathbf{H}^T \mathbf{R}^{-1} \mathbf{H} + \mathbf{Q}_0^{-1}) \mathbf{v}_1^k = \mathbf{H}^T \mathbf{R}^{-1} \mathbf{y} + \mathbf{Q}_0^{-1} \mathbf{v}_0 + (\mathbf{H}^T \mathbf{R}^{-\frac{1}{2}}, \mathbf{L}^{-1}) \boldsymbol{\epsilon}_k, \quad \boldsymbol{\epsilon}_k \sim \mathcal{N}(\mathbf{0}, \mathbf{I}_{M+N}), \quad (5.7)$$

is a sample from the Gaussian distribution $\mathcal{N}(\mathbf{v}_1, \mathbf{Q}_1)$ with \mathbf{v}_1 and \mathbf{Q}_1 according to (5.3) and (5.2). The matrix \mathbf{L} denotes the Cholesky factorization of the matrix $\mathbf{Q}_0 = \mathbf{L} \mathbf{L}^T$ such that $\mathbf{Q}_0^{-1} = \mathbf{L}^{-T} \mathbf{L}^{-1}$.

Proof. Again we make use of the linearity of the expected value function, to show that

$$\mathbb{E}(\mathbf{v}_1^k) = \mathbf{Q}_1 (\mathbf{H}^T \mathbf{R}^{-1} \mathbf{y} + \mathbf{Q}_0^{-1} \mathbf{v}_0) = \mathbf{v}_1,$$

and

$$\begin{aligned} \mathbb{E}((\mathbf{v}_1^k - \mathbb{E}(\mathbf{v}_1^k))(\mathbf{v}_1^k - \mathbb{E}(\mathbf{v}_1^k))^T) &= \mathbb{E}(\mathbf{v}_1^k \mathbf{v}_1^{k,T}) - \mathbb{E}(\mathbf{v}_1^k) \mathbb{E}(\mathbf{v}_1^k)^T \\ &= \mathbf{v}_1 \mathbf{v}_1^T + \mathbf{Q}_1 \underbrace{(\mathbf{H}^T \mathbf{R}^{-1} \mathbf{H} + \mathbf{Q}_0^{-1}) \mathbf{Q}_1 - \mathbf{v}_1 \mathbf{v}_1^T}_{= \mathbf{Q}_1^{-1}} = \mathbf{Q}_1. \quad \square \end{aligned}$$

Remark 10. The noise covariance matrix $\mathbf{R} \in \mathbb{R}^{M \times M}$ may be of high dimension, but sparse, since the measurements between the moves are uncorrelated. We make use of the Cholesky module for sparse matrices (SimplicialLLT) implemented in the Eigen C++ library [18] for the factorization according to $\mathbf{R} = \mathbf{R}^{\frac{1}{2}} (\mathbf{R}^{\frac{1}{2}})^T$, where $\mathbf{R}^{\frac{1}{2}}$ is lower triangular. The term $\mathbf{R}^{-1} \mathbf{H}$ can then be computed efficiently by backward substitution.

Approximating the posterior covariance matrix by an ensemble of K state vectors with $K \ll N$ can be considered as a compression technique to reduce the computational effort significantly. This advantage is further enhanced by the use of fast algorithms for the computations of the products $\mathbf{H}\mathbf{v}$, e.g., the fast multipole method.

In Figure 6, we illustrate the posterior covariance matrix approximated for different ensemble sizes K and also the case of a direct inversion of \mathbf{Q}_1^{-1} . In this case $M = 4093$ measurement positions were taken with the Hall probe mapper system. The finite sampling size introduces sampling errors, which appear as spurious correlations. This is a well-known phenomenon in ensemble methods (see [14]). However it is not harmful for the field evaluation inside the domain, particularly in the vicinity of the particle beam, because details in the matrix \mathbf{Q}_1 are smoothed out when evaluating the boundary integral equation. This is shown in Figure 7, where the uncertainty in the evaluation of B_y evaluated along a reference trajectory is shown.

Remark 11. The convergence of the posterior covariance matrix for $K \rightarrow \infty$ is studied in [27]. It is shown in [24] and [16] that, without further treatment, the required ensemble size to obtain a bounded error growth of the covariance matrix, is proportional to the square of the system dimension. As a treatment, covariance-shrinking

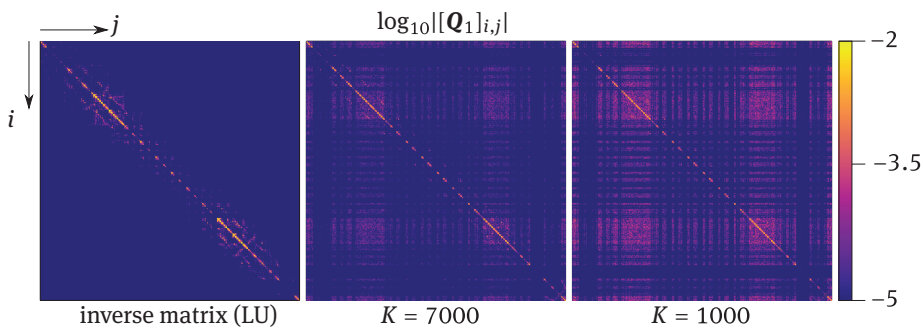


Figure 6: Elements of the posterior covariance matrix in logarithmic scale. See Section 4 for details about the experiment. Here $M = 4093$ measurement positions were collected. Left: The covariance matrix was computed from direct inversion of the matrix \mathbf{Q}_1^{-1} using the LU-solver implemented in Eigen [18]. Center and right: The covariance matrix was approximated from $K = 7000$ and 1000 samples \mathbf{v}_k . The approximation is visible by sampling errors, i.e. spurious covariances.

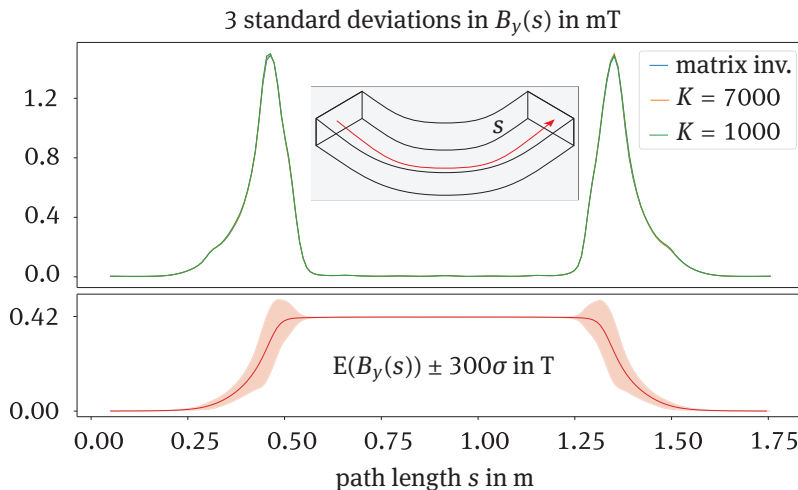


Figure 7: Uncertainty in the field reconstruction along a reference trajectory s , measured in three standard deviations. The reconstruction is based on the covariance matrices given in Figure 6. Top: (blue) The uncertainty is evaluated by the normal transformation $\mathbf{H}\mathbf{Q}_1\mathbf{H}^T$, where \mathbf{Q}_1 was computed by direct inversion and \mathbf{H} is the observation operator for B_y . (orange and green): The covariance matrix is approximated from $K = 7000$ and 1000 samples. It is found that the approximation of the covariance matrix according to Figure 6 is not harmful for the uncertainty quantification at the reference trajectory. This is due to the smoothing property of the boundary integral equation. Bottom: The red line shows the mean value of $B_y(s)$. The red contour illustrates the uncertainty, whereas, for better visualization, the standard deviation was multiplied by a factor 300.

and tapering methods are applied in sampling based Kálmán filtering (see the discussions in [16] and the references therein). Absolute estimates for the optimal ensemble sizes K are problem dependent. Some studies have been performed in [33] and [14]. Evidence has shown that a small ensemble, typically of size $K = 100$, is sufficient for many applications in the geosciences [4]. In the following, we choose $K = 1000$ because it yields the required reduction in computational complexity and memory, to perform the analysis on standard desktop computers. Moreover, Figure 7 provides evidence that the sampling errors are not harmful for the uncertainty quantification along the reference particle trajectory.

5.2 The Ensemble Kálmán Filter

The equations for the Kálmán filter require the inverse of the prior covariance matrix \mathbf{Q}_0 to be accessible. In a high-dimensional setting they are therefore only applicable for simple prior covariance models, such as identity or sparse matrices, but also the covariance matrix which will be presented in Section 5.3.

In the case of the *ensemble Kálmán filter*, the prior and posterior covariance matrices are represented by ensembles of state vectors. In this way a significant reduction of computational complexity can be achieved.

Similarly to (5.7) the ensemble Kálmán filter is based on a randomized linear equation system. The proof for the following statement is completely analogous to the one provided for Theorem 4 and it is found in [13].

Proposition 2. *The state vector \mathbf{v}_1^k with*

$$\mathbf{v}_1^k = \mathbf{v}_0^k + \mathbf{K}(\mathbf{y}^k - \mathbf{H}\mathbf{v}_0^k) \quad (5.8)$$

where $\mathbf{y}^k \sim \mathcal{N}(\mathbf{y}, \mathbf{R})$ and $\mathbf{v}_0^k \sim \mathcal{N}(\mathbf{v}_0, \mathbf{Q}_0)$, is a sample from the posterior distribution $p(\mathbf{v}|\mathbf{y}) \sim \mathcal{N}(\mathbf{v}_1, \mathbf{Q}_1)$, with \mathbf{v}_1 and \mathbf{Q}_1 according to (5.4) and (5.5).

The following equations summarize the analysis step of the ensemble Kálmán filter as they are well known in the field of data assimilation (see for instance [4], [13] or [14]). The ensemble Kálmán filter follows from Proposition 2 after estimating the mean and covariance of the prior \mathbf{v}_0 according to

$$\mathbb{E}(\mathbf{v}_0) \approx \frac{1}{K} \sum_{k=1}^K \mathbf{v}_0^k, \quad \mathbf{Q}_0 \approx \frac{\mathbf{U}\mathbf{U}^T}{K-1} \quad \text{with} \quad \mathbf{U} = \mathbf{V}_0 - \mathbb{E}(\mathbf{v}_0)\mathbf{I}_{1 \times K}. \quad (5.9)$$

The update step can then be performed directly on the ensemble $\mathbf{V}_0 := (\mathbf{v}_0^1, \dots, \mathbf{v}_0^K) \in \mathbb{R}^{N \times K}$ and the *data matrix* $\mathbf{Y} := (\mathbf{y}^1, \dots, \mathbf{y}^K) \in \mathbb{R}^{3M \times K}$, via the equations

$$\mathbf{V}_1 = \mathbf{V}_0 + \frac{1}{K-1} \mathbf{U}(\mathbf{H}\mathbf{U})^T \mathbf{P}^{-1}(\mathbf{Y} - \mathbf{H}\mathbf{V}_0), \quad \mathbf{P} := \frac{1}{K-1} \mathbf{H}\mathbf{U}(\mathbf{H}\mathbf{U})^T + \mathbf{R} \in \mathbb{R}^{3M \times 3M}. \quad (5.10)$$

The matrix $\mathbf{V}_1 = (\mathbf{v}_1^1, \dots, \mathbf{v}_1^K)$ stores the posterior ensemble. The statistics of the posterior distribution can be computed from the sampled mean and covariance of the posterior ensemble (see (5.9)).

In the case of a non-linear observation operator \mathbf{H} , or when the observation operator is available in compressed form only, a matrix-free implementation is possible. One therefore defines the matrices $\mathbf{H}\mathbf{V}_0$ and $\mathbf{H}\mathbf{U}$ according to

$$\mathbf{H}\mathbf{V}_0 := (\mathbf{H}(\mathbf{v}_0^1), \dots, \mathbf{H}(\mathbf{v}_0^K)), \quad (5.11)$$

$$\mathbf{H}\mathbf{U} := (\mathbf{H}(\mathbf{v}_0^1) - \mathbb{E}(\mathbf{H}(\mathbf{v}_0^1)), \dots, \mathbf{H}(\mathbf{v}_0^K) - \mathbb{E}(\mathbf{H}(\mathbf{v}_0^K))), \quad (5.12)$$

where

$$\mathbb{E}(\mathbf{H}(\mathbf{v}_0^k)) := \frac{1}{N} \sum_{k=1}^K \mathbf{H}(\mathbf{v}_0^k). \quad (5.13)$$

Remark 12. Working with a nonlinear observation operator in ensemble Kálmán filtering comes with approximation errors, as the true nonlinear update is fitted with a Gaussian model. In complex high-dimensional problems of data assimilation, the ensemble Kálmán filter is still popular, as it is often the only way to perform approximate inference, and alternative techniques can only be applied to highly simplified versions of the original problem [23].

In this work the ensemble Kálmán filter is used to update the prior ensemble \mathbf{V}_0 in regions of the magnet where the remaining uncertainty is large. Compared to the dimension of the state vector N , less measurements are used for such local updates. The \mathbf{P} matrix is therefore of a size $M \ll N$. For high-dimensional updates $M \gg N$, it is shown in [30] how to reformulate \mathbf{P} to obtain a linear complexity in M .

5.3 The Prior

Due to the smoothing property of the boundary integral equation, the inverse problem is ill-conditioned. To ensure a numerically stable solution we derive a regularization term which is based on a prior field solution. It is now shown how mean \mathbf{v}_0 and covariance \mathbf{Q}_0 of a Gaussian prior $p(\mathbf{v}) \sim \mathcal{N}(\mathbf{v}_0, \mathbf{Q}_0)$ can be computed from a numerical field simulation.

From (2.5) we derive the randomized indirect Neumann problem:

$$\mathbf{D}\mathbf{v}_0 = \mathbf{f} + \boldsymbol{\epsilon}_p, \quad \boldsymbol{\epsilon} \sim \mathcal{N}(\mathbf{0}, \delta^{-\frac{1}{2}} \mathbf{I}_{N \times N}). \quad (5.14)$$

The *process noise* $\boldsymbol{\epsilon}_p$ is used to impose uncertainty in the field simulation. From the linearity of the expected value function it follows

$$\mathbf{v} \sim \mathcal{N}(\underbrace{\mathbf{D}^{-1}\mathbf{f}}_{=: \mathbf{v}_0}, \underbrace{\delta^{-1}\mathbf{D}^{-1}\mathbf{D}^{-1}}_{=: \mathbf{Q}_0}), \quad (5.15)$$

due to the symmetry of \mathbf{D} .

Equation (5.15) provides a Gaussian prior $p(\mathbf{v})$, with covariance matrix $\mathbf{Q}_0 = \delta^{-1}\mathbf{D}^{-1}\mathbf{D}^{-1}$. In this context, the discretized hypersingular operator \mathbf{D} already provides the square root of matrix \mathbf{Q}_0^{-1} . It therefore ties in nicely with equation (5.7). As an alternative to (5.7) it is possible to solve (5.14) for K realizations of $\boldsymbol{\epsilon}_p^k$ to generate an initial ensemble and use it for the ensemble Kálmán filter.

The *regularization parameter* δ controls the impact of the prior. Since $\mathbf{Q}_0^{-1} = \delta\mathbf{D}\mathbf{D}$, all terms related to the prior in (5.7) vanish for $\delta \rightarrow 0$. It then holds a proportionality relation between the likelihood and the posterior. This prior is *not informative* and it may be considered as choosing a sufficiently flat pdf such that $p(\mathbf{v}) \approx \text{constant}$ in Bayes rule (5.1).

On the other hand, the prior state vector \mathbf{v}_0 is recovered in the limit $\delta \rightarrow \infty$. This can be seen when dividing (5.7) by δ and substituting $\mathbf{Q}_0^{-1} = \delta\mathbf{D}\mathbf{D}$ such that

$$(\delta^{-1}\mathbf{H}^T\mathbf{R}^{-1}\mathbf{H} + \mathbf{D}\mathbf{D})\mathbf{v}_1^k = \delta^{-1}\mathbf{H}^T\mathbf{R}^{-1}\mathbf{y} + \mathbf{D}\mathbf{D}\mathbf{v}_0 + (\delta^{-1}\mathbf{H}^T\mathbf{R}^{-\frac{1}{2}}, \delta^{-\frac{1}{2}}\mathbf{D})\boldsymbol{\epsilon}_p^k \xrightarrow{\delta \rightarrow \infty} \mathbf{D}\mathbf{D}\mathbf{v}_1^k = \mathbf{D}\mathbf{D}\mathbf{v}_0. \quad (5.16)$$

The parameter δ has the same role as the *ridge parameter* in the Tikhonov regularization. Different approaches have been developed for its selection (see for instance [1, Chapter 1]). In the following we make use of a set of validation measurements, providing us with the vector $\mathbf{y}_{\text{val}} \in \mathbb{R}^{3M_{\text{val}}}$ and we select δ according to

$$\delta = \arg \min_{\delta^*} \epsilon(\delta^*) := \arg \min_{\delta^*} \frac{1}{\sqrt{3M_{\text{val}}}} \|\mathbf{y}_{\text{val}} - \mathbf{E}(\mathbf{H}_{\text{val}}\mathbf{v}_{\delta^*})\|, \quad (5.17)$$

where \mathbf{v}_{δ^*} is computed from (5.16) using $\delta = \delta^*$, \mathbf{H}_{val} is the observation operator for the validation set and $\mathbf{E}(\cdot)$ is the expected value function. By this definition ϵ is the root-mean-squared (RMS) error between the predicted mean and the validation measurements.

In Figure 8 (right), the validation error $\epsilon(\delta^*)$ is shown in a logarithmic scale, for two scenarios. The results have been obtained from the application discussed in Section 4. Whereas only $M = 4093$ measurements have been collected in the first scenario, in the second one, we have taken measurements at $M = 16\,324$ positions. The validation errors saturate at $(3M)^{-\frac{1}{2}} \|\mathbf{y}_{\text{val}} - \mathbf{H}_{\text{val}}(\mathbf{v}_0)\|^2$ for $\delta \rightarrow \infty$ in both cases. This is the RMS error of the prior field solution. On the other hand, the rank of the matrix $\mathbf{H}^T\mathbf{R}^{-1}\mathbf{H}$ determines the validation errors for $\delta \rightarrow 0$. For the case $M = 4093$ this matrix is rank-deficient, while for the second scenario, more data is available and $\epsilon(\delta^*)$ saturates at the *maximum likelihood solution*. The values for δ^* minimizing the validation errors are found in Table 2. A-priori estimates for δ that avoid the validation set are discussed in [1, Chapter 1].

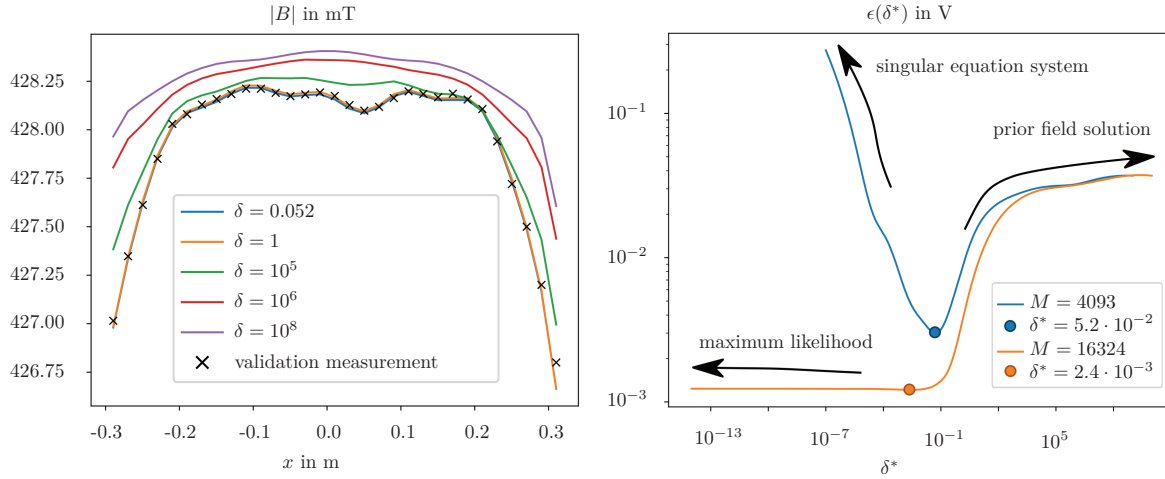


Figure 8: Left: Prediction of $|B|$ along the x -axis in the magnet center, for different values of the regularization parameters, compared to a validation measurement, here $M = 4093$. Right: The validation error over δ^* in logarithmic scale for both scenarios.

Scenario	Moves	M	Measurement Resolution h_{meas}	Measurement Duration	Regularization Parameter δ
1	281	4093	24 mm	0.5 h	$5.2 \cdot 10^{-2}$
2	562	16324	6 mm	2 h	$2.4 \cdot 10^{-3}$

Table 2: Parameters related to the initialization measurement.

5.4 Design of Experiment

Design of experiment is about determining the minimum amount of measurements required to meet the accuracy requirements. As we have seen in the previous section, the number of measurements, their spatial distribution and also the prior $E(v_0)$ determine the matrix $H^T R(E(v_0))^{-1} H$, which is equivalent to the inverse of the posterior covariance matrix for $\delta = 0$.

Using the procedure developed in the previous sections, we are capable to propagate the measurement uncertainty down to beam related quantities by particle tracking. In the following, we consider the trajectory of a proton with momentum $P_0 = 100$ MeV/c, for a single passage through the magnet as the quantity of interest.

This trajectory is illustrated in Figure 9, which shows the solution of (2.13) for a reference particle using an explicit, fourth-order Runge–Kutta scheme for the numerical integration (see [20, Chapter 2]).

Remark 13. The explicit Runge–Kutta scheme is not symplectic, meaning that the Hamiltonian H , which is an invariant of motion, is not preserved by the numerical integration scheme. With the expression for the magnetic vector potential by means of (2.4), it is possible to use symplectic numerical integrators for multi-turn particle simulations, which are preserving the Hamiltonian by design (see [20, Chapter 6]). A comprehensive study of different numerical integration schemes is found in [42]). The use of spherical harmonics in symplectic particle tracking has been presented in [2]. The chosen procedure serves to illustrate the potential of our method. More detailed analyses of the numerical integration are planned for future publications.

We have calculated the trajectory for $K = 1000$ ensembles of the posterior, based on the ensemble generated from the scenario $M = 16324$. The uncertainty in the fringe field region results in 3 standard deviations of $51 \mu\text{m}$ for the prediction of the x -coordinate at the exit of the magnet. For comparison, a constant deviation in the vertical flux density B_y of one unit in 10 000 with respect to the maximum field, gives a total deviation in the trajectory radius of $108 \mu\text{m}$. The uncertainty of $51 \mu\text{m}$ is therefore acceptable for many applications.

In contrast to the posterior covariance matrix, the validation error cannot be determined a-priori. It mainly originates from locations in the fringe fields, where the spatial resolution of 6 mm is not sufficient to properly resolve the differences between prior and posterior. As a mitigation measure, update measurements are taken

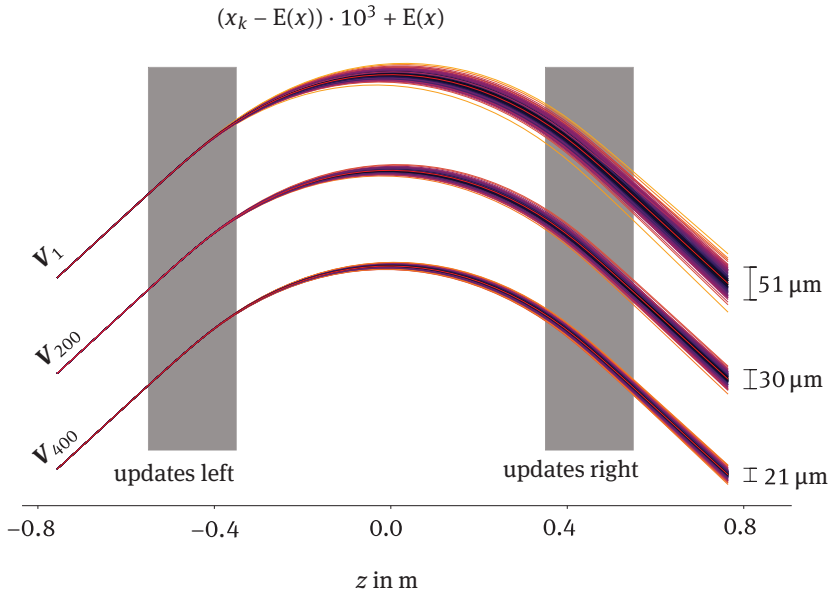


Figure 9: Prediction of the particle trajectory for different stages of the ensemble Kálmán filter. The deviations from the mean trajectory were amplified by a factor of 1000 for better visualization. The deviations are representing the uncertainty in the particle trajectory due to the measurement uncertainty in the fringe fields. First $M = 16324$ measurements were taken with the Hall probe mapper system and the trajectory was evaluated from $K = 1000$ samples from the posterior (V_1). Update measurements in the left and right-hand side of the magnet (gray) were performed to reduce the validation error and also the precision in the particle trajectory. This yields the ensembles V_{200} and V_{400} . A proton with momentum $P_0 = 100$ MeV/c is considered. This corresponds to the injection energy of the ELENA ring.

	Prior V_0	Initialization V_1	Updates Left V_{200}	Updates Right V_{400}
ϵ in mV	37.01	5.04	3.86	2.01
Equivalent B in mT	7.40	1.00	0.77	0.401

Table 3: RMS validation errors.

at these positions. In order to avoid moving the stages back and forth between the left and the right-hand side of the magnet, both sides of the magnet are treated individually.

The initial ensemble is updated move-by-move, using the equations of the ensemble Kálmán filter with $K = 1000$. We denote the posterior ensemble of update j by V_j . We have performed a total of $J = 400$ update measurements equally distributed between left and right-hand side. These updates provide us with the posterior ensembles V_{200} and V_{400} , which are the results after treating the left and right-hand side of the magnet.

Table 3 gives the resulting validation errors. By means of the ensemble Kálmán updates, the validation error was reduced by a factor 2.5. As a side effect, more measurement data increases the precision in the prediction of the particle trajectory. This is shown in Figure 9, where we have added the trajectories evaluated from the posterior ensembles V_{200} and V_{400} .

6 Conclusion

We have developed an approach that improves the performance of Hall probe field mapping in several aspects: The measurement duration to obtain a three-dimensional field map could be reduced from $\mathcal{O}(1/h_{\text{meas}}^3)$ to $\mathcal{O}(1/h_{\text{meas}})$. This could be achieved by using a boundary element method for the field reconstruction based on measured boundary data and taking the measurements on-the-fly, while moving the stages of the Hall probe mapper system. The last aspect unfortunately has the consequence that vibrations and position errors become unavoidable. These errors are most harmful in the fringe field region. For this reason a rigorous treatment

of these effects was proposed and it was shown how to propagate the uncertainties all the way to the prediction of the particle beam trajectory. Moreover, it was shown how successive Bayesian updates can be selected efficiently, in order to improve the precision of the model predictions.

To achieve these goals we have used an iso-geometric boundary-element method based on an indirect double-layer potential formulation. In terms of applicability, we emphasized the scalability of the algorithms and presented a method for efficient evaluation of the integral equation along the reference trajectory.

For the inference of boundary data from magnetic measurements we have made use of ensemble Kálmán filter, which provides us with an efficient compression technique of the posterior covariance matrix. This yields a significant reduction in computational complexity.

Acknowledgment: The authors thank Thomas Zickler for providing the OPERA model of the ELENA bending dipole magnet and Dimitrios Loukrezis and Lucio Fiscarelli for reviewing and discussing this article.

Funding: The work of Melvin Liebsch is supported by the Graduate School CE within the Centre for Computational Engineering at Technische Universität Darmstadt.

References

- [1] J. M. Bardsley, *Computational Uncertainty Quantification for Inverse Problems*, Comput. Sci. Eng. 19, Society for Industrial and Applied Mathematics, Philadelphia, 2018.
- [2] L. Bojtár, Efficient evaluation of arbitrary static electromagnetic fields with applications for symplectic particle tracking, *Nucl. Instrum. Methods Phys. Res. A* **948** (2019), Article ID 162841.
- [3] A. Buffa, J. Dölz, S. Kurz, S. Schöps, R. Vázquez and F. Wolf, Multipatch approximation of the de Rham sequence and its traces in isogeometric analysis, *Numer. Math.* **144** (2020), no. 1, 201–236.
- [4] A. Carrassi, M. Bocquet, L. Bertino and G. Evensen, Data assimilation in the geosciences - an overview on methods, issues and perspectives, *WIREs Climate Change* **9** (2017), DOI 10.1002/wcc.535.
- [5] B. Dalena, O. Gabouev, J. Payet, Antoine Chance, D. R. Brett, R. B. Appleby, R. DeMaria and M. Giovannozzi, Fringe fields modeling for the high luminosity LHC large aperture quadrupoles, in: *Proceedings of the 5th International Particle Accelerator Conference (IPAC 2014)*, JACoW Publishing, Geneva (2014), 993–996.
- [6] J. Dölz, H. Harbrecht, C. Jerez-Hanckes and M. Multerer, Isogeometric multilevel quadrature for forward and inverse random acoustic scattering, *Comput. Methods Appl. Mech. Engrg.* **388** (2022), Paper No. 114242.
- [7] J. Dölz, H. Harbrecht, S. Kurz, M. Multerer, S. Schöps and F. Wolf, Bembel: Boundary element method based engineering library, 2022.
- [8] J. Dölz, H. Harbrecht and M. Peters, \mathcal{H} -matrix accelerated second moment analysis for potentials with rough correlation, *J. Sci. Comput.* **65** (2015), no. 1, 387–410.
- [9] J. Dölz, H. Harbrecht and M. Peters, An interpolation-based fast multipole method for higher-order boundary elements on parametric surfaces, *Internat. J. Numer. Methods Engrg.* **108** (2016), no. 13, 1705–1728.
- [10] A. Dragt, T. J. Stasevich and P. Walstrom, Computation of charged-particle transfer maps for general fields and geometries using electromagnetic boundary-value data, in: *Proceedings of the 2001 Particle Accelerator Conference (PACS2001)*, IEEE Press, Piscataway (2001), 1776–1777.
- [11] A. J. Dragt, F. Neri, G. Rangarajan, D. R. Douglas, L. M. Healy and R. D. Ryne, Lie algebraic treatment of linear and nonlinear beam dynamics, *Ann. Rev. Nuclear Particle Sci.* **38** (1988), no. 1, 455–496.
- [12] A. Ern and J.-L. Guermond, *Theory and Practice of Finite Elements*, Appl. Math. Sci. 159, Springer, New York, 2013.
- [13] G. Evensen, The ensemble Kalman filter: Theoretical formulation and practical implementation, *Ocean Dynam.* **53** (2003), no. 4, 343–367.
- [14] G. Evensen, Spurious correlations, localization, and inflation, in: *Data Assimilation*, Springer, Berlin (2009), 237–253.
- [15] P. Förster, S. Schöps, J. Enders, M. Herbert and A. Simona, Freeform shape optimization of a compact dc photoelectron gun using isogeometric analysis, *Phys. Rev. Accel. Beams* **25** (2022), Article ID 034601.
- [16] R. Furrer and T. Bengtsson, Estimation of high-dimensional prior and posterior covariance matrices in Kalman filter variants, *J. Multivariate Anal.* **98** (2007), no. 2, 227–255.
- [17] L. Greengard and V. Rokhlin, A new version of the fast multipole method for the Laplace equation in three dimensions, *Acta Numer.* **6** (1997), 229–269.
- [18] G. Guennebaud, B. Jacob, Eigen v3, <http://eigen.tuxfamily.org>, 2010.
- [19] E. Hairer, *Geometric Numerical Integration: Structure-Preserving Algorithms for Ordinary Differential Equations*, Springer, Berlin, 2006.

- [20] E. Hairer, C. Lubich and G. Wanner, *Geometric Numerical Integration: Structure-Preserving Algorithms for Ordinary Differential Equations*, 2nd ed., Springer Ser. Comput. Math. 31, Springer, Berlin, 2006.
- [21] I. G. Ion, M. Liebsch, A. Simona, D. Loukrezis, C. Petrone, S. Russenschuck, H. De Gersem and S. Schöps, Local field reconstruction from rotating coil measurements in particle accelerator magnets, *Nucl. Instrum. Methods Phys. Res. A* **1011** (2021), Article ID 165580.
- [22] I. G. Ion, C. Wildner, D. Loukrezis, H. Koepl and H. De Gersem, Tensor-train approximation of the chemical master equation and its application for parameter inference, *J. Chem. Phys.* **155** (2021), no. 3, Article ID 034102.
- [23] M. Katzfuss, J. R. Stroud and C. K. Wikle, Understanding the ensemble Kalman filter, *Amer. Statist.* **70** (2016), no. 4, 350–357.
- [24] H. R. Künsch, State space and hidden Markov models, in: *Complex Stochastic Systems* (Eindhoven 1999), Monogr. Statist. Appl. Probab. 87, Chapman & Hall/CRC, Boca Raton (2001), 109–173.
- [25] S. Kurz, H. De Gersem, A. Galetzka, A. Klaedtke, M. Liebsch, D. Loukrezis, S. Russenschuck and M. Schmidt, Hybrid modeling: Towards the next level of scientific computing in engineering, *J. Math. Indust.* **12** (2022), Article ID 8.
- [26] S. Kurz, D. Pauly, D. Praetorius, S. Repin and D. Sebastian, Functional a posteriori error estimates for boundary element methods, *Numer. Math.* **147** (2021), no. 4, 937–966.
- [27] F. Le Gland, V. Monbet and V.-D. Tran, Large sample asymptotics for the ensemble Kalman filter, Research Report RR-7014, INRIA, 2009.
- [28] G. Lehner and S. Kurz, *Electromagnetic Field Theory for Engineers and Physicists*, Springer, Berlin, 2010.
- [29] Y. Liu, *Fast Multipole Boundary Element Method: Theory and Applications in Engineering*, Cambridge University, Cambridge, 2009.
- [30] J. Mandel, Efficient implementation of the ensemble Kalman filter, UCDHSC/CCM Report no. 231, University of Colorado at Denver and Health Sciences Center, 2006.
- [31] R. Nertens, U. Pahner, K. Hameyer, R. Belmans and R. De Weerd, Force calculation based on a local solution of Laplace's equation, *IEEE Trans. Magnetics* **33** (1997), no. 2, 1216–1218.
- [32] W. Oelert, The ELENA project at CERN, *Acta Phys. Polonica B* **46** (2015), Article ID 181.
- [33] E. Ott, B. R. Hunt, I. Szunyogh, A. V. Zimin, E. J. Kostelich, M. Corazza, E. Kalnay, D. J. Patil and J. A. Yorke, A local ensemble Kálmán filter for atmospheric data assimilation, *Tellus A Dyn. Meteorol. Oceanography* **56** (2004), no. 5, 415–428.
- [34] Y. Papaphilippou, J. Wei and R. Talman, Deflections in magnet fringe fields, *Phys. Rev. E* **67** (2003), Article ID 046502.
- [35] S. Rjasanow and O. Steinbach, *The Fast Solution of Boundary Integral Equations*, Springer, New York, 2007.
- [36] S. Russenschuck, *Field Computation for Accelerator Magnets*, Wiley-VCH, Weinheim, 2010.
- [37] S. Russenschuck, Rotating- and translating-coil magnetometers for extracting pseudo-multipoles in accelerator magnets, *COMPEL* **36** (2017), no. 5, 1552–1567.
- [38] S. A. Sauter and C. Schwab, *Boundary Element Methods*, Springer Ser. Comput. Math. 39, Springer, Berlin, 2011.
- [39] D. Schoerling, Design study: ELENA bending magnet prototype, Report CERN-ACC-2013-0261, CERN, Geneva, 2013.
- [40] J. Sherman and W. J. Morrison, Adjustment of an inverse matrix corresponding to a change in one element of a given matrix, *Ann. Math. Statistics* **21** (1950), 124–127.
- [41] A. Simona, *Numerical methods for the simulation of particle motion in electromagnetic fields*, PhD thesis, Politecnico di Milano, Milano, 2020.
- [42] A. Simona, L. Bonaventura, T. Pugnati and B. Dalena, High order time integrators for the simulation of charged particle motion in magnetic quadrupoles, *Comput. Phys. Commun.* **239** (2019), 33–52.
- [43] S. Sorti, C. Petrone, S. Russenschuck and F. Braghin, A magneto-mechanical model for rotating-coil magnetometers, *Nucl. Instrum. Methods Phys. Res. A* **984** (2020), Article ID 164599.
- [44] M. Spink, D. Claxton, C. de Falco and R. Vázquez, The NURBS toolbox, <http://octave.sourceforge.net/nurbs/index.html>.
- [45] O. Steinbach, *Numerical Approximation Methods for Elliptic Boundary Value Problems*, Springer, New York, 2008.
- [46] M. Venturini, D. Abell and A. Dragt, Map computation from magnetic field data and application to the LHC high-gradient quadrupoles, 1999.
- [47] A. Wolski, *Beam Dynamics in High Energy Particle Accelerators*, Imperial College, London, 2014.
- [48] Y. K. Wu, E. Forest and D. Robin, Explicit symplectic integrator of s-dependent static magnetic field, *Phys. Rev. E* **68** (2003), Article ID 046502.
- [49] International Organization for Standardization, Guide to the expression of uncertainty in measurement (GUM)-Supplement 1: Numerical methods for the propagation of distributions, volume ISO draft guide DGUIDE99998, International Organization for Standardization, Geneva, 2004.
- [50] NIST Digital Library of Mathematical Functions, <http://dlmf.nist.gov/>, Release 1.1.3 of 2021-09-15, F. W. J. Olver, A. B. Olde Daalhuis, D. W. Lozier, B. I. Schneider, R. F. Boisvert, C. W. Clark, B. R. Miller, B. V. Saunders, H. S. Cohl, and M. A. McClain.